High Metallicity and Non-Equilibrium Chemistry in the Dayside Atmosphere of Hot-Neptune Gj 436b

Citation: Madhusudhan, N., and S. Seager. "High Metallicity and Non-Equilibrium Chemistry in the Dayside Atmosphere of Hot-Neptune Gj 436b." The Astrophysical Journal 729.1 (2011): 41. © 2011 IOP Publishing

As Published: http://dx.doi.org/ 10.1088/0004-637x/729/1/41

Publisher: IOP Publishing

Persistent URL: http://hdl.handle.net/1721.1/74099

Version: Final published version: final published article, as it appeared in a journal, conference proceedings, or other formally published context

The Astrophysical Journal, 729:41 (13pp), 2011 March 1 doi:10.1088/0004-637X/729/1/41

HIGH METALLICITY AND NON-EQUILIBRIUM CHEMISTRY IN THE DAYSIDE ATMOSPHERE OF HOT-NEPTUNE GJ 436b

N. Madhusudhan[1] and S. Seager[1,2]
[1] MIT Kavli Institute for Astrophysics and Space Research, and Department of Earth, Atmospheric, and Planetary Sciences, MIT, Cambridge, MA 02139, USA; nmadhu@mit.edu
[2] Department of Physics, MIT, Cambridge, MA 02139, USA
Received 2010 April 28; accepted 2010 December 21; published 2011 February 8

ABSTRACT

We present a detailed analysis of the dayside atmosphere of the hot-Neptune GJ 436b, based on recent *Spitzer* observations. We report statistical constraints on the thermal and chemical properties of the planetary atmosphere, study correlations between the various molecular species, and discuss scenarios of equilibrium and non-equilibrium chemistry in GJ 436b. We model the atmosphere with a one-dimensional line-by-line radiative transfer code with parameterized molecular abundances and temperature structure. We explore the model parameter space with 10^6 models, using a Markov chain Monte Carlo scheme. Our results encompass previous findings, indicating a paucity of methane, an overabundance of CO and CO_2, and a slight underabundance of H_2O, as compared to equilibrium chemistry with solar metallicity. The concentrations of the species are highly correlated. Our best-fit, and most plausible, constraints require a CH_4 mixing ratio of 10^{-7} to 10^{-6}, with CO $\geqslant 10^{-3}$, $CO_2 \sim 10^{-6}$ to 10^{-4}, and $H_2O \leqslant 10^{-4}$; higher CH_4 would require much higher CO and CO_2. Based on calculations of equilibrium and non-equilibrium chemistry, we find that the observed abundances can potentially be explained by a combination of high metallicity ($\sim$10$\times$ solar) and vertical mixing with $K_{zz} \sim 10^6$–10^7 cm^2 s^{-1}. The inferred metallicity is enhanced over that of the host star which is known to be consistent with solar metallicity. Our constraints rule out a dayside thermal inversion in GJ 436b. We emphasize that the constraints reported in this work depend crucially on the observations in the two *Spitzer* channels at 3.6 μm and 4.5 μm. Future observations with warm *Spitzer* and with the *James Webb Space Telescope* will be extremely important to improve upon the present constraints on the abundances of carbon species in the dayside atmosphere of GJ 436b.

Key words: planetary systems – planets and satellites: general – planets and satellites: individual (GJ 436b) – radiative transfer

Online-only material: color figures

1. INTRODUCTION

The last decade in exoplanetary science has demonstrated our capability in detecting and characterizing atmospheres of transiting extrasolar giant planets. Several observations have been reported using the *Hubble Space Telescope* (*HST*), *Spitzer Space Telescope* (*Spitzer*), and from the ground. Beginning with the first detection of sodium in the atmosphere of HD 209458b in transit (Charbonneau et al. 2002) and the first detections of dayside thermal emission from hot Jupiters TrES-1 and HD 209458b (Charbonneau et al. 2005; Deming et al. 2005), atmospheric observations of giant exoplanets today are a norm, albeit still very challenging (e.g., Knutson et al. 2008; Charbonneau et al. 2008; Swain et al. 2008; Grillmair et al. 2008; Desert et al. 2009; Swain et al. 2009a). The intensity of observational efforts has been matched with equally challenging accomplishments in theoretical modeling of exoplanet atmospheres and data interpretation (Seager & Sasselov 2000; Seager et al. 2005; Burrows et al. 2006, 2008; Fortney et al. 2006; Barman et al. 2005; Tinetti et al. 2007; Showman et al. 2009; Madhusudhan & Seager 2009). Several inferences of gaseous H_2O, CH_4, CO, and CO_2, and thermal inversions have subsequently been made in hot-Jupiter atmospheres (Burrows et al. 2007; Tinetti et al. 2007; Barman 2007; Grillmair et al. 2008; Swain et al. 2008; Madhusudhan & Seager 2009; Swain et al. 2009a, 2009b).

A new era in exoplanetary science has now dawned. The latest observations are leading to discovery and characterization of transiting exoplanets much less massive than the archetypal hot Jupiters, namely, extrasolar Neptunes and super-Earths. Several low-mass transiting planets are presently known, e.g., hot-Neptunes GJ 436b (Butler et al. 2004; Maness et al. 2007), HAT-P-11b (Bakos et al. 2010), HAT-P-26b (Hartman et al. 2010), and Kepler-4b (Borucki et al. 2010), and super-Earths CoRoT-7b (Leger et al. 2009) and GJ 1214b (Charbonneau et al. 2009). These planets have opened a new regime in atmospheric modeling and data interpretation. However, observations of thermal emission have been reported for only one of these planets so far, GJ 436b (Deming et al. 2007, Stevenson et al. 2010).

The first transiting hot Neptune known, GJ 436b, with a mass of 22.6 $M_\oplus$ and radius of 4.2 $R_\oplus$, orbits an M Dwarf at an orbital separation of 0.03 AU (Butler et al. 2004; Gillon et al. 2007; Maness et al. 2007). The host star has an effective temperature of about 3500 K and a metallicity consistent with solar (Torres et al. 2008). The average density of the planet is 1.5 g/cc (Torres et al. 2008), i.e., similar to the bulk density of Neptune, an ice giant. At an equilibrium temperature of $\sim$700 K, assuming zero albedo and efficient energy circulation, the density originally hinted at a hot-ice interior (Gillon et al. 2007). More detailed studies of the possible bulk composition of GJ 436b indicate that an additional layer of the H/He atmosphere would be needed to account for the observed radius (Figueira et al. 2009; Rogers & Seager 2009).

The atmosphere of GJ 436b has been the subject of substantial interest in the recent past. Deming et al. (2007) and Demory

et al. (2007) reported independent detections of thermal emission from the day side of GJ 436b in the *Spitzer* 8 μm IRAC channel. Although no meaningful inferences about the molecular compositions can be drawn from a single data point, model fits to the 8 μm flux contrast have favored the interpretation of inefficient day–night energy redistribution for GJ 436b (Demory et al. 2007; Spiegel et al. 2010; unless there are additional unknown optical absorbers in the atmosphere). The models used in Demory et al. 2007 and Spiegel et al. 2010 had assumed equilibrium chemistry. Given the low temperatures of GJ 436b compared to hot Jupiters, equilibrium chemistry suggests that the planet's atmosphere must be abundant in methane and water vapor, and be scarce in carbon monoxide (e.g., Burrows & Sharp 1999).

Recent observations have suggested distinct departures from predictions of equilibrium chemistry models. Pont et al. (2009) reported a transmission spectrum of GJ 436b obtained in the 1.1–1.9 μm bandpass using the *HST* NICMOS instrument, but found no significant feature in the 1.4 μm water band; the spectrum was flat at the 2σ uncertainties. More recently, Stevenson et al. (2010) reported planet–star flux contrasts of the dayside atmosphere of GJ 436b in six channels of *Spitzer* broadband photometry, and inferred a deficiency of methane in the atmosphere of GJ 436b, using models based on Madhusudhan & Seager (2009) and the present work. The high planet–star flux contrast observed in the 3.6 μm IRAC channel was central to the low methane requirement. Even though our models do not assume equilibrium chemistry, the inferred methane mixing ratio of $\sim 10^{-7}$ in a hydrogen-dominated atmosphere at $\sim$700 K signals a surprising new regime in atmospheric chemistry of extrasolar planets.

In this work, we report detailed statistical constraints on the atmospheric properties of GJ 436b, and explore channels of equilibrium and non-equilibrium chemistry that might explain the observed chemical abundances. We first estimate the atmospheric chemical composition and temperature structure at different levels of fit to the data, using a one-dimensional (1D) line-by-line radiative transfer model for exoplanet atmospheres (Madhusudhan & Seager 2009). Our constraints result from exploring the model parameter space with $\sim 10^6$ models, optimized using a Markov chain Monte Carlo optimization scheme. We then use detailed calculations of equilibrium and non-equilibrium chemistry, and with different metallicities, to explain the observed constraints on the various molecular species.

Our results indicate that high metallicity and non-equilibrium chemistry are required to explain the molecular abundances constrained by the observations. The requirement of non-equilibrium chemistry is consistent with our findings in Stevenson et al. (2010). The observations require the presence of CO and CO_2 and a substantial depletion of CH_4 in the dayside atmosphere of GJ 436b. In this work, we find that the constraints on the CO and CO_2 mixing ratios can be explained by vertical mixing in the atmosphere (with $K_{zz} \sim 10^6$–10^7 cm^2 s^{-1}) and a high metallicity (10$\times$ solar). And, we suggest that the low CH_4 required can potentially be explained by non-equilibrium chemistry. We also find that the observations require inefficient day–night energy redistribution in GJ 436b, which can be confirmed by future observations of phase curves.

In what follows, we first give a brief overview of the model-independent interpretation of *Spitzer* observations in Section 2. We then describe our atmosphere model, the parameter space optimization scheme, and the models for equilibrium and non-equilibrium chemistry we use in this work in Section 3. We present the results of our analysis in Section 4. Finally, in Section 5, we present a summary of our work and discuss consequences for future observations and theoretical models.

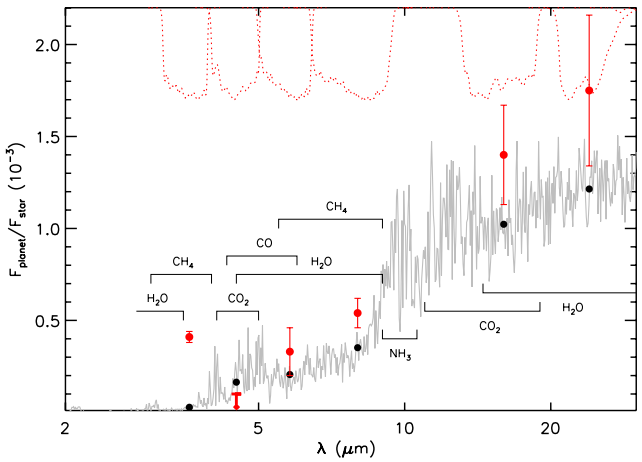

Figure 1. Molecular absorption features in *Spitzer* photometric bandpasses. The red dotted lines at the top show the six *Spitzer* bandpasses. The black lines show the extent of absorption features due to the corresponding molecules. The gray curve shows a hypothetical model spectrum of GJ 436b based on equilibrium chemistry, and the black filled circles show the corresponding integrated points in the *Spitzer* channels. The red filled circles with error bars show the observations of GJ 436b reported by Stevenson et al. (2010).

(A color version of this figure is available in the online journal.)

2. OVERVIEW OF *SPITZER* DATA INTERPRETATION

The concentrations of major molecular species in an exoplanetary atmosphere can be constrained to some extent from observations in the six channels of *Spitzer* photometry, at 3.6 μm, 4.5 μm, 5.8 μm, 8 μm, 16 μm, and 24 μm. Figure 1 illustrates the spectral features of the dominant molecules in the *Spitzer* channels, for a synthetic thermal spectrum of GJ 436b. CH_4 has strong features almost exclusively in the 3.6 μm and 8 μm channels. CO has a strong feature in the 4.5 μm channel, also contributing to the 5.8 μm channel. And, CO_2 has strong features in the 4.5 μm and 16 μm channels. Although H_2O has several spectral features in most of the *Spitzer* channels, the stronger and/or unique features lie in the 3.6 μm, 5.8 μm, and 24 μm channels. Given the strong features of the molecules in one or more *Spitzer* channels, reasonable constraints can be placed with high signal-to-noise ratio (S/N) observations. In principle, however, the presence of additional species in significant amounts, due to non-equilibrium chemistry (e.g., Zahnle et al. 2009b) and non-LTE effects (Swain et al. 2010), can also affect the emergent spectrum. We discuss these factors in Section 3.1.

The constraints on the atmospheric properties that might be possible from high S/N *Spitzer* photometry can be understood in light of the key parameters affecting the emergent spectrum (Madhusudhan & Seager 2009). Under the assumption that H_2O, CH_4, CO, and CO_2 are the dominant, spectroscopically-active molecules in the *Spitzer* bands, the molecular concentrations constitute four free parameters. And, although the temperature structure can involve many free parameters, the temperature at the base of the atmosphere (at $P \sim$ 1–10 bar) and the thermal gradient are the two most important parameters, in the absence of a thermal inversion. Apart from the data themselves, an additional constraint on the parameters appear in the form of energy balance (discussed in Section 3.1). Thus, the six observations can potentially lead to meaningful constraints on the six key

atmospheric parameters, mainly on the four dominant molecules. These same molecular species can then provide constraints on the C/H and O/H ratios in the atmosphere.

As an example of constraining molecular abundances from the *Spitzer* data, consider a planetary atmosphere with $T_{eq} \sim$ 700–1000 K and a temperature profile decreasing outward (i.e., no thermal inversion). Further suppose that a low thermal flux is observed in the 3.6 μm channel. Such a low flux would suggest strong absorption due to a high concentration of methane. And, if the low 3.6 μm flux is indeed due to a high methane abundance (since water vapor also absorbs weakly in the 3.6 μm channel), the flux should also be low in the 8 μm channel where methane also absorbs strongly (as shown, for example, by the black filled circles in Figure 1). On the other hand, high planet fluxes in the 3.6 and 8 μm channels indicate low absorption due to methane, and hence a paucity of methane in the planet atmosphere.

A second example concerns constraining the molecular abundances of CO and CO_2. A low flux observed in the 4.5 μm channel must indicate atmospheric absorption due to CO and/or CO_2. At 4.5 μm, CO_2 has a stronger absorption cross-section than CO, so that a small concentration of CO_2 can produce an absorption feature comparable to that from a relatively large concentration of CO. The degeneracy between CO and CO_2 contributions in a 4.5 μm measurement can be broken by an observation in the 16 μm channel, where only CO_2 contributes, between the two. As a third example, constraints on H_2O are based primarily on fluxes in the 5.8 μm and 24 μm channels. An important note concerns the presence of a thermal inversion in the atmosphere, a region where temperature increases outward. In such a case, the molecular features would be emission features instead of absorption features, thus reversing the logic of inferences described above (Madhusudhan & Seager 2010).

The recent observations of the dayside atmosphere of GJ 436b by Stevenson et al. (2010) represent a quintessential example of the above inferences. Their observations indicate an extremely high flux in the 3.6 μm channel and an extremely low flux in the 4.5 μm channel, causing a brightness temperature differential of ~450 K between the two adjacent channels. Thus, following the arguments described above, the observations point towards an extremely low methane abundance and high CO and/or CO_2 abundances, for a temperature profile without a thermal inversion. This identification of low CH_4 and high CO and/or CO_2 was in fact the central result of Stevenson et al. (2010), based on a more elaborate atmospheric modeling procedure, also discussed in the present work. We emphasize that, although the six channels of photometry can yield statistical constraints on the atmospheric properties, they cannot yield a unique solution, given the large number of free parameters (Madhusudhan & Seager 2009).

3. MODEL

Our goal is to determine the best-fitting interpretation for observations of the dayside atmosphere of GJ 436b. We first fit the data with a large ensemble of 1D dayside atmosphere models of GJ 436b, and determine regions of the parameter space that fit the data best. Our results yield best-fit constraints on the molecular abundances and temperature structure. We then use some of the best-fit temperature profiles, along with independent calculations of equilibrium and non-equilibrium chemistry to see if we can explain the observed constraints on the molecular abundances.

3.1. Radiative Transfer Model

In order to fit the observations with model spectra, we use the 1D exoplanetary atmosphere model developed in Madhusudhan & Seager (2009). Our model consists of a line-by-line radiative transfer code, with constraints of hydrostatic equilibrium and global energy balance, and coupled to a parametric pressure–temperature (*P–T*) structure and parametric molecular abundances. This modeling approach allows one to compute large ensembles of models, and to explore efficiently the parameter space of molecular abundances and temperature structure.

The major difference of our model from traditional 1D atmosphere models is in the treatment of energy balance. Our model requires energy balance at the top of the atmosphere, instead of an iterative scheme to ensure layer-by-layer radiative (or radiative + convective) equilibrium which is assumed in conventional models (e.g., Seager et al. 2005; Burrows et al. 2006; Fortney et al. 2006). For a given set of model parameters, we require that the net energy output at the top of the atmosphere is less than or equal to the net energy input due to the incident stellar flux; a deficit indicates energy redistributed to the night side. Models where the emergent flux exceeds the incident flux are discarded (see Madhusudhan & Seager 2009).

In this work, we consider well mixed atmospheres, i.e., uniform mixing ratio of each molecular species over the entire atmosphere. The present approach allows us to sample a wider range of compositions independent of any assumptions of equilibrium chemistry. The molecular species in our models include molecular hydrogen (H_2), water vapor (H_2O), carbon monoxide (CO), carbon dioxide (CO_2), and methane (CH_4). We have used an alternate approach in previous works (e.g., Madhusudhan & Seager 2009), where we parameterized the abundances in terms of deviations from equilibrium chemistry. We find that the constraints on the overall mixing ratios do not depend critically on the choice of parameterization. Our H_2O, CH_4, and CO molecular line data are from Freedman et al. (2008) and references therein. Our CO_2 data are from R. S. Freedman (2009, private communication) and Rothman et al. (2005). And, we obtain the H_2–H_2 collision-induced opacities from Borysow et al. (1997) and Borysow (2002).

Our model does not include effects of non-LTE radiative transfer. Models of exoplanetary spectra with non-LTE radiative transfer calculations have not been reported. Recently, Swain et al. (2010) reported detection of excess emission at 3.25 μm in a ground-based thermal spectrum of HD 189733b, which they surmised to be due to non-LTE methane emission. However, follow-up observations by Mandell et al. (2010) failed to detect the feature reported by Swain et al. (2010). Furthermore, their estimates of potential contribution from resonant florescence, a non-LTE emission mechanism, of methane yielded fluxes too low to significantly contribute to the emission spectrum, contrary to the observations of Swain et al. (2010). Nevertheless, detailed atmospheric models of GJ 436b in the future might need to account for non-LTE contributions to spectra, as high-resolution observations become possible in the future with the *James Webb Space Telescope* (*JWST*).

We also do not include in our list of molecules higher hydrocarbons that might be potential byproducts of non-equilibrium chemistry. Non-equilibrium chemistry can lead to hydrocarbons like C_2H_2 and C_2H_4, depending on the temperature and degree of vertical mixing (Zahnle et al. 2009b; Line et al. 2010). However, as will be discussed in Section 4.2.2, the observations of GJ 436b indicate high temperatures ($T \gtrsim$ 1100 K) at 1–10 bar pressures, thereby favoring the oxidation of CH_4 to CO

over conversion of CH_4 to higher hydrocarbons (Zahnle et al. 2009b). Nevertheless, constraining these species observationally would still be a worthwhile exercise when higher resolution observations become available with the *JWST*.

3.2. Parameter Space Exploration for Model Fits

We use the Markov chain Monte Carlo (MCMC) method to explore the model parameter space. The MCMC method is a Bayesian parameter estimation algorithm which allows the calculation of posterior probability distributions of the model parameters conditional to a given set of observations, and prior probabilities (see, e.g., Tegmark et al. 2004; Ford 2005). In this work, our goal is not parameter estimation—the number of model parameters ($N = 10$) exceeds the number of available observations ($N_{\rm obs} = 6$) and renders the problem underconstrained. However, the MCMC method allows an efficient means of exploring the parameter space in search of regions which provide the best fits to the observations. We, therefore, use the MCMC method with a Metropolis–Hastings scheme within the Gibbs sampler, for fine sampling of the model parameter space. We also report error contours in the space of the molecular compositions and temperature structure. Our statistic of choice is ξ^2, defined as $\chi^2/N_{\rm obs}$ (Madhusudhan & Seager 2009). In this metric, $\xi^2 = 1$ indicates models fitting the observations within the 1σ observational uncertainties, on average. Similarly, ξ^2 of 2 and 3 indicate fits at the 1.41σ (i.e., $\sqrt{2}$) and 1.73σ error bars, respectively.

Our model described in Section 3.1 above has ten free parameters (Madhusudhan & Seager 2009). Six parameters concern the *P*–*T* profile: T_0, P_1, P_2, P_3, α_1, and α_2. Four parameters correspond to the uniform molecular mixing ratios: $f_{\rm H_2O}$, $f_{\rm CO}$, $f_{\rm CH_4}$, and $f_{\rm CO_2}$. We define the mixing ratio of a molecule as the number fraction with respect to molecular hydrogen.

We define some physically motivated boundaries in the parameter space explored by the Markov chain. We restrict all the molecular mixing ratios to the range of $[10^{-10}, 0.1]$. We also impose the constraint of global energy balance by restricting η to [0.0,1.0], where $\eta = (1 - A)(1 - f_r)$ is the ratio of emergent flux output on the day side to incident stellar flux input on the day side, weighted appropriately (Madhusudhan & Seager 2009). Here, A is the bond albedo and f_r is the day–night energy redistribution. The "fit" parameters for the MCMC are T_0, $\log(P_1)$, $\log(P_2)$, $\log(P_3)$, α_1, α_2, $\log(f_{\rm H_2O})$, $\log(f_{\rm CO})$, $\log(f_{\rm CH_4})$, and $\log(f_{\rm CO_2})$. We consider uniform priors in all the parameters. For each system under consideration, we run one chain of 10^6 links, which takes ~22 hr on a single processor.

3.3. Chemistry Model

After we obtain the constraints on the molecular abundances from model fits to data, we investigate processes of atmospheric chemistry that could explain the required abundances. Atmospheres of giant planets in the solar system and those of brown dwarfs have revealed the interplay between equilibrium and non-equilibrium chemical processes in hydrogen-rich atmospheres (Prinn & Bashay 1977; Fegley & Lodders 1994; Noll et al. 1997; Saumon et al. 2006). At high pressures deep in a planetary atmosphere, molecules react fast enough that all species are in thermochemical equilibrium. As the pressures decrease with increasing altitude, thermochemical reaction rates decrease, allowing for competing non-equilibrium processes with shorter timescales to shift the involved species out of equilibrium. We compute the atmospheric compositions in equilibrium using the equilibrium chemistry code adapted from Seager et al. (2005).

3.3.1. Equilibrium Chemistry

Our objective here is to determine whether the observed constraints on the molecular mixing ratios are consistent with chemical equilibrium. To this end, we calculate the equilibrium compositions of the species using the equilibrium chemistry code originally developed in Seager et al. (2000), and subsequently used in Seager et al. (2005) and Miller-Ricci et al. (2009). We calculate the gas phase molecular mixing ratios for 172 molecules, resulting from abundances of 23 atomic species, by minimizing the net Gibbs free energy of the system. The multi-dimensional Newton–Raphson method described in White et al. (1958) was used for the minimization. We adopt polynomial fits for the free energies of the molecules, based on Sharp & Huebner (1990). We assume a hydrogen-dominated atmosphere for GJ 436b, and we compute equilibrium concentrations of all the species at varying metallicities (see Section 4.1), over a grid in pressure and temperature.

At the temperatures of GJ 436b, the most abundant and spectroscopically active molecules in the *Spitzer* bandpasses are expected to be H_2O, CH_4, CO, and CO_2. Ammonia (NH_3) should also be abundant, but does not contain major features in the *Spitzer* channels. At high temperatures, e.g., $\gtrsim$1300 K at 1 bar pressure, like those in hot-Jupiter atmospheres, CO is predicted to be the dominant carbon and oxygen bearing species. At lower temperatures, on the other hand, CH_4 is the dominant carbon bearing species in equilibrium. Water vapor is a major carrier of oxygen in either regime. The specific amounts of each of these species also depend strongly on the assumed metallicity, and pressure. Finally, the amount of carbon dioxide in equilibrium is a very strong function of metallicity. At the temperatures of GJ 436b, solar metallicity yields a CO_2 mixing ratio up to 10^{-7}, whereas amounts as high as 10^{-4} can be obtained for 30× solar metallicity.

3.3.2. Non-equilibrium Chemistry

Vertical mixing can drive species out of equilibrium in regions of the atmosphere where the timescale of vertical transport is shorter compared to the timescale governing chemical equilibrium between the relevant species. At high pressures, deep in the atmosphere, convection is a natural mixing mechanism. However, above the radiative-convective boundary, atmospheric instabilities and turbulent processes, such as wave breaking, can also lead to vertical motions. This form of mixing in the radiative zone is collectively termed as "eddy mixing" or "eddy diffusion," and is parameterized as a diffusion process, with a coefficient of eddy diffusion (K_{zz}). Such mixing shifts molecular species, in radiative regions, away from their equilibrium concentrations. Eddy mixing has been known in the context of atmospheres of solar system giant planets (Prinn & Bashay 1977; Fegley & Lodders 1994) and brown dwarfs (Noll et al. 1997; Saumon et al. 2003, 2006; Hubeny & Burrows 2007). Cooper & Showman (2006) studied eddy mixing in hot-Jupiter atmospheres. Eddy mixing offers a viable explanation to the excess carbon monoxide discovered in hydrogen-dominated atmospheres (see, e.g., Yung & Demore 1999). The primary reaction governing the relative abundances of CH_4 and CO in equilibrium is given by

$$\mathrm{CO} + 3\mathrm{H_2} \rightleftharpoons \mathrm{CH_4} + \mathrm{H_2O}. \quad (1)$$

This reaction favors CO at high temperatures and CH_4 at the low temperatures of GJ 436b. Thus, based on equilibrium chemistry, it is expected for CO to be dominant in the hotter lower regions of the atmosphere ($T \gtrsim 1200$ K), and CH_4 to be dominant at higher altitudes where temperatures are lower ($T \lesssim 1000$ K). However, atmospheric spectra of solar system planets and cooler brown dwarfs suggest significant amounts of CO in the upper layers of the atmosphere (see, e.g., Fegley & Lodders 1994; Noll et al. 1997; Stephens et al. 2009). This is achieved by eddy mixing; which vertically transports CO from the lower regions of an atmosphere to the upper regions.

Eddy mixing dominates when the mixing timescale ($\tau_{\rm mix}$) is shorter than the chemical timescale ($\tau_{\rm chem}$) of CO in the forward reaction in Equation (1). The forward reaction in Equation (1) in fact proceeds via multiple steps, and Yung et al. (1988) suggested the rate determining step in the reaction chain to be (but cf. Visscher et al. 2010):

$$\mathrm{H} + \mathrm{H_2CO} + \mathrm{M} \rightarrow \mathrm{CH_3O} + \mathrm{M}. \quad (2)$$

The lifetime of CO is given by

$$\tau_{\rm chem} \sim \frac{[\mathrm{CO}]}{d[\mathrm{CO}]/dt} = \frac{[\mathrm{CO}]}{k_f [\mathrm{H}][\mathrm{H_2CO}]}, \quad (3)$$

where k_f is the rate constant for the forward reaction. k_f is not known directly, but can be estimated from the reverse reaction rate constant (k_r), which is known from laboratory experiments, and the equilibrium constant ($K_{\rm eq}$) for the reaction (see Griffith & Yelle 1999 for a detailed discussion). In the present study, we use the following estimate of k_f, based on Line et al. (2010):

$$k_f = 3.07 \times 10^{-12}\, T^{-1.2} e^{(3927/T)}. \quad (4)$$

Then, $\tau_{\rm chem}$ can be calculated from Equation (3), using equilibrium concentrations of CO, H, and H_2CO.

The mixing time ($\tau_{\rm mix}$) in radiative regions of the atmosphere is determined by the eddy diffusion coefficient (K_{zz}) and a characteristic length scale for mixing (L) as

$$\tau_{\rm mix} \sim \frac{L^2}{K_{zz}}. \quad (5)$$

L is typically chosen to be the scale height (H; e.g., Prinn & Bashay 1977; Line et al. 2010). However, for the coolest of giant planets, like Jupiter, L can be as low as $0.1H$ (Smith 1998). In this work, we choose $L = H$; a lower L does not significantly alter our results, as discussed in Section 4.2.1.

As is evident from the above discussion, both $\tau_{\rm mix}$ and $\tau_{\rm chem}$ vary with height in the atmosphere, although $\tau_{\rm mix}$ varies to a lesser extent than $\tau_{\rm chem}$. But, while $\tau_{\rm chem}$ increases towards higher levels in the atmosphere (i.e., with decreasing pressure), $\tau_{\rm mix}$ increases in the opposite direction. The pressure (p_0) at which $\tau_{\rm mix} = \tau_{\rm chem}$ is called the "quench" level. Above this pressure, i.e., in deeper layers of the atmosphere, the species are in chemical equilibrium, and below this pressure the concentration of the species (CO in this case) is fixed, or "quenched," at the equilibrium value at p_0. This yields a uniform mixing ratio profile for the species for pressures below p_0.

Thus, a higher p_0 implies that CO can be dredged up from deeper levels in the atmosphere, and, since in equilibrium CO concentration increases with pressure, a high p_0 implies higher concentration of CO in the upper layers of the atmosphere. It can be shown that, for a given $\tau_{\rm chem}$ profile, p_0 increases monotonically with K_{zz}, thus correlating a high CO concentration in the upper atmosphere with a high K_{zz} (see, e.g., Griffith & Yelle 1999). In the discussion here, we have assumed a temperature profile that increases monotonically with pressure. The dependence of observed CO on K_{zz} deviates from this monotonic behavior for more complicated temperature structures, for example, in the presence of thermal inversions or partial isotherms, as will be shown in Section 4.2.

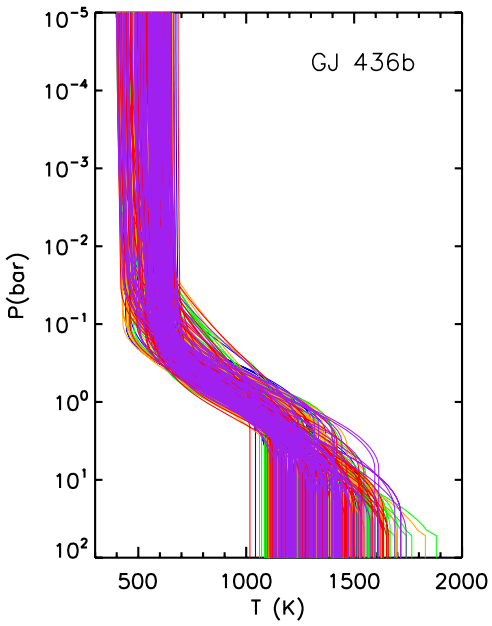

Figure 2. Pressure–temperature (P–T) profiles of GJ 436b. The purple, red, orange, green, and blue profiles correspond to models which fit the observations to within ξ^2 of 1.0, 2.0, 3.0, 4.0, and 5.0, respectively.

(A color version of this figure is available in the online journal.)

In this work, we explore the CO mixing ratios resulting from different combinations of K_{zz} and metallicities. We explore values of K_{zz} between 10^2 and 10^{10}, and metallicities of solar—30× solar. Our choices of metallicities are motivated by the constraints on CO and CO_2 abundances which indicate high C/H and O/H ratios a priori. Our range in K_{zz} encompasses values found in solar system planets and brown dwarfs. For comparison, planetary atmospheres in the solar system have K_{zz} ranging between 10^5 and 10^9 cm^2 s^{-1}, and K_{zz} for brown dwarf atmospheres can be as low as 10^2–10^4 cm^2 s^{-1} (Prinn & Bashay 1977; Yung & Demore 1999; Saumon et al. 2003).

4. RESULTS

In this section, we present constraints on the atmospheric properties of the dayside atmosphere of GJ 436b, as placed by the six channel *Spitzer* photometry. We first report constraints on the molecular abundances and discuss the correlations between the various species. We then discuss the physical plausibility of the solutions and present calculations of equilibrium and non-equilibrium chemistry attempting to explain the observed constraints. Finally, we present constraints on the atmospheric temperature structure and day–night energy redistribution. Our constraints follow from a detailed exploration of the model parameter space with $\sim 10^6$ models, using the procedures described in Section 3.2.

Our modeling approach allows the placing of statistically robust model constraints from the data. The pressure–temperature (P–T) profiles explored by our models are shown in Figure 2, color coded by their degree of fit to data. The goodness-of-fit

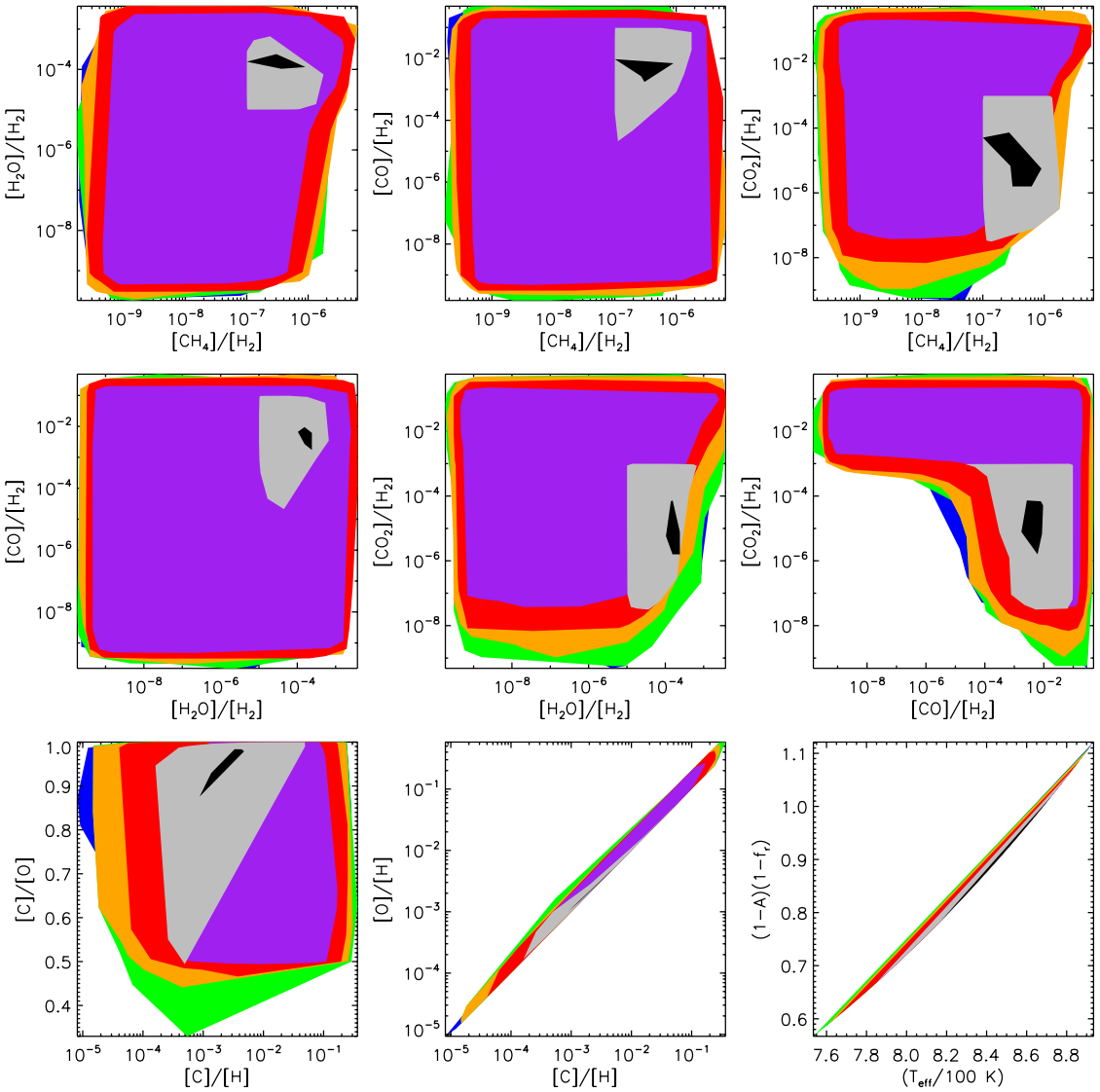

Figure 3. Constraints on the atmospheric properties of GJ 436b. Mixing ratios are shown as ratios by number density. The contours show surfaces of minimum ξ^2 in the space of atmospheric composition and temperature structure. The purple, red, orange, green, and blue correspond to minimum ξ^2 of 1.0, 2.0, 3.0, 4.0, and 5.0, respectively. The gray and black regions correspond to models which have methane mixing ratios greater than 10^{-7}, along with different conditions on the compositions of the remaining molecules, and allowing fits within $\xi^2 = 3$. For the gray surfaces, $CO_2 \leqslant 10^{-3}$, $H_2O \geqslant 10^{-5}$, and $CO \leqslant 10^{-1}$. CO_2 of $\sim 10^{-3}$ and CO of $\sim 10^{-1}$ are implausible either in equilibrium or non-equilibrium chemistry (Lodders & Fegley 2002; Zahnle et al. 2009a); however, we show these solutions for completeness. The black surfaces show solutions within more plausible limits (see Section 4.1.1) of $CO_2 \leqslant 10^{-4}$, $H_2O \geqslant 10^{-4}$, and $CO \leqslant 10^{-2}$. The black contour in the C/H–O/H plane requires C/H and O/H $\geqslant 10\times$ solar abundances.

(A color version of this figure is available in the online journal.)

contours in the space of atmospheric composition are shown in Figure 3. As mentioned in Section 3.2, our statistic for the goodness of fit is given by (Madhusudhan & Seager 2009)

$$\xi^2 = \frac{1}{N_{\rm obs}} \sum_{i=1}^{N_{\rm obs}} \left(\frac{f_{i,\rm model} - f_{i,\rm obs}}{\sigma_{i,\rm obs}} \right)^2, \quad (6)$$

where $f_{i,\rm model}$ is the planet–star flux contrast of the model in each channel, and $f_{i,\rm obs}$ and $\sigma_{i,\rm obs}$ are the observed flux contrast and the 1σ uncertainty in that channel, respectively. $N_{\rm obs}$ is the number of observations. Here, $N_{\rm obs} = 6$, corresponding to the six channels of *Spitzer* photometry. In this metric, a $\xi^2 = 1$ indicates models fitting the observations within the 1σ observational uncertainties, on average. Similarly, ξ^2 of 2 and 3 indicate fits at the 1.41σ (i.e., $\sqrt{2}$) and 1.73σ error bars, respectively.

The constraints depend on the ξ^2 surface one chooses for interpretation, apart from any conditions of physical plausibility one would like to impose on the models. We first report constraints at the $\xi^2 = 1$ and $\xi^2 = 2$ levels, and with only the barest assumptions of physical plausibility. We then discuss additional constraints that result from considering some nominal conditions of physical plausibility, from equilibrium and non-equilibrium chemistry.

4.1. Constraints on Chemical Composition

The constraints on the molecular abundances are strongly influenced by the correlations between them. The correlations between the molecules result from their overlapping absorption features in the *Spitzer* channels as described in Section 2. We present constraints on the mixing ratios of methane (CH_4), water vapor (H_2O), carbon monoxide (CO), and carbon dioxide (CO_2).

Because the abundances of molecules are correlated, constraints on any molecule have to be discussed with respect to abundances of one or more of the remaining molecules.

The constraints on all the molecules and the correlations between them are shown in Figure 3.

Methane (CH_4). Our results indicate a substantial paucity of methane in the dayside atmosphere of GJ 436b. Our results place an absolute upper limit on the mixing ratio of methane to be 3×10^{-6} to 6×10^{-6}, for ξ^2 ranging between 1 and 5, and assuming nothing about the remaining molecules. However, these upper limits allow for a wide range of abundances of the remaining molecules, including some manifestly impractical values. Primarily, the constraints include CO_2 abundances as high as 0.3, implying that 30% of a hydrogen-dominated atmosphere is composed of CO_2. Assuming high metallicity for the planet atmosphere (about 30× solar), CO_2 mixing ratios as high as $\sim 10^{-4}$ can be attained by equilibrium chemistry, as shown in Figure 5 (see also Zahnle et al. 2009a, 2009b).

The methane mixing ratio is constrained to values below 10^{-6}, if we impose plausible limits on the CO_2 abundance. A generous upper limit on the CO_2 abundance can be assumed to be $\sim 10^{-3}$, based on the arguments above. Allowing a maximum CO_2 of 10^{-3}, at the $\xi^2 \leqslant 1$ surface (purple surfaces in Figure 3) the methane mixing ratio is constrained to between 10^{-7} and 10^{-6}, for CO_2 mixing ratios between 10^{-7} and 10^{-3}. And, at the $\xi^2 \leqslant 2$ surface (red surfaces in Figure 3), $CH_4 = 10^{-7}$ to 10^{-6} for $CO_2 = 10^{-8}$ to 10^{-3}. There is no lower bound on the CH_4 abundance; mixing ratios below 10^{-9} do not have discernible features at the resolution of the current data.

The low methane requirement is enforced primarily by the high planet–star flux contrast in the 3.6 μm *Spitzer* IRAC channel. Inflating the uncertainties in the 3.6 μm channel does not obviate the low methane requirement. The strong correlation of methane with CO_2 arises from the large flux differential between the 3.6 μm and 4.5 μm channels, as has been described in Section 2. Methane is also correlated with water vapor which also has features in the 3.6 μm channel, albeit to a lesser extent, as shown in Figure 3.

The low mixing ratio of methane is a clear indication of non-equilibrium chemistry in the dayside atmosphere of GJ 436b, as has been suggested in Stevenson et al. (2010). Equilibrium chemistry at the temperatures of GJ 436b causes methane to be a dominant carbon bearing molecule. At solar abundances the methane mixing ratio in chemical equilibrium, for typical temperature profiles of GJ 436b, is predicted to be 7×10^{-4}, and 2×10^{-2} for 30× solar abundances, as is evident from Figure 5.

Water vapor (H_2O). Our results place an absolute upper limit on the H_2O abundance, as shown in Figure 3. The H_2O mixing ratio is constrained to $< 10^{-3}$ and $< 3 \times 10^{-3}$ for $\xi^2 \leqslant 1$ and $\xi^2 \leqslant 5$, respectively, if we make no assumptions about the physical plausibility of the solutions. As in the case of methane, however, the H_2O abundance is also correlated with the CO_2 abundance. If we restrict CO_2 to a generous upper limit of 10^{-3}, as described for the case of methane, the $\xi^2 \leqslant 1$ and $\xi^2 \leqslant 2$ surfaces constrain the H_2O abundance to $< 3 \times 10^{-4}$ and $<10^{-3}$, respectively. H_2O is also correlated with CO and CH_4. Thus, the H_2O abundance can be further constrained if we assume conditions of physical plausibility of all the species simultaneously (discussed below in Section 4.1.1). The correlations of H_2O with all the remaining molecules arise from its numerous features in all the *Spitzer* channels, as described in Section 2.

Carbon monoxide (CO). The abundance of CO is highly correlated with the abundance of CO_2. If no assumption is made on the CO_2 abundance, the observations provide no constraint on the CO mixing ratio, as shown in Figure 3. If the mixing ratio of CO_2 is restricted to the conservative upper limit of 10^{-3}, the observations constrain CO to be $\geqslant 3 \times 10^{-5}$ for $\xi^2 < 1$, while still leaving it unconstrained at $\xi^2 \sim 2$ and higher.

Despite the constraints on CO above, simultaneous conditions of physical plausibility on all the molecules indicate that a very high CO abundance ($\geqslant 10^{-3}$) is essential to explain the observations. This will be discussed in Section 4.1.1 below. The strong correlation between CO and CO_2 arises from the fact that both molecules have strong features in the 4.5 μm IRAC channel, the CO_2 feature being stronger, as described in Section 2. Although not apparent in Figure 3, CO is also correlated with H_2O and CH_4, via their correlations with CO_2.

Carbon dioxide (CO_2). The observations require a clear presence of CO_2 in the atmosphere, as shown in Figure 3. Since CO_2 and CO are correlated, a low concentration of CO_2 requires a high concentration of CO. At the $\xi^2 \leqslant 1$ surface, a CO_2 concentration less than 10^{-7} requires a CO concentration greater than 10^{-2}. On the other hand, having a CO_2 concentration of 10^{-4} allows for CO concentrations as low as $\sim 10^{-3}$, at the $\xi^2 \leqslant 1$ surface. For ξ^2 surfaces of 2 and higher, lower CO abundances can fit the data for a given CO_2 abundance, as shown in Figure 3. However, CO_2 is also correlated with H_2O, such that an H_2O abundance greater than 3×10^{-4} would require a CO_2 abundance greater than $\sim 10^{-4}$, at the $\xi^2 \leqslant 1$ surface.

The observations themselves do not place any upper limit on the CO_2 abundance. However, the maximum amount of CO_2 possible can be constrained based on theoretical limits of equilibrium and non-equilibrium chemistry. For the best-fit temperature profiles of GJ 436b shown in Figure 2 and pressures in the 10^{-3} to 1 bar range, thermochemical equilibrium can yield CO_2 mixing ratios up to 10^{-7} for solar metallicity and up to 10^{-4} for ∼30× solar metallicities (see Figure 5). The strong dependence of CO_2 abundance on metallicity has been reported before (Lodders & Fegley 2002; Zahnle et al. 2009a).

4.1.1. Plausibility of the Abundance Constraints

The constraints reported above assume nothing with regards to the physical plausibility of the models, except for the conservative limit of $CO_2 \leqslant 10^{-3}$ used for the sake of argument. However, reasonable theoretical constraints can be placed over the observed constraints based on well established arguments of equilibrium and non-equilibrium chemistry (see Section 3.3). The mixing ratios of CH_4, H_2O, CO, and CO_2 under chemical equilibrium are shown in Figure 5, for a range of temperatures and pressures pertinent to GJ 436b, along with some best-fit *P*–*T* profiles. A detailed discussion of non-equilibrium chemistry, via eddy mixing, is presented in Section 4.2.

We find that stringent constraints on the molecular abundances required by the data can be placed even with modest assumptions of atmospheric chemistry. As alluded to in Section 4.1 above, and shown in Figure 5, CO_2 mixing ratios up to 10^{-4} are allowed for high metallicity (also see Zahnle et al. 2009a; Lodders & Fegley 2002). H_2O is a major carrier of oxygen in the desired temperature range. The H_2O mixing ratio is expected to be $\sim 10^{-4}$ and $\sim 5 \times 10^{-3}$ for solar and 30× solar abundances, respectively. And, while there is no lower limit on the CO abundance, the CO upper limit is fixed by the metallicity; CO $\lesssim 10^{-4}$ and $\lesssim 10^{-2}$ for solar and 30× solar abundances,

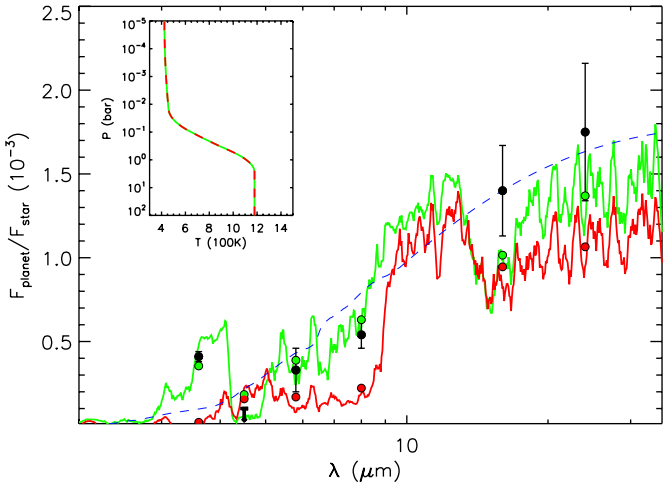

Figure 4. Observations and model spectra for dayside emission from GJ 436b. The black filled circles with error bars show the *Spitzer* observations in the six photometric channels, from Stevenson et al. (2010). The blue dashed lines shows a planet blackbody spectra at 800 K. The green and red curves show two model spectra, and the colored circles show the corresponding channel integrated model points. The green model is a best-fit model spectrum (see Section 4.1.1), with non-equilibrium molecular mixing ratios of $H_2O = 10^{-4}$, $CO = 7 \times 10^{-3}$, $CH_4 = 10^{-6}$, and $CO_2 = 6 \times 10^{-6}$. The red model has a composition close to chemical equilibrium with solar abundances, with $H_2O = 2 \times 10^{-3}$, $CO = 10^{-5}$, and $CH_4 = 7 \times 10^{-4}$; it also contains $CO_2 = 10^{-6}$. Both models have the same pressure–temperature profile, shown in the inset. The green, non-equilibrium model has a maximum day–night energy redistribution fraction (f_r) of 0.03, i.e., for zero bond albedo (A_B). On the other hand, the red, equilibrium model has very efficient redistribution, $f_r \leqslant 0.63$, for $A_B = 0$.

(A color version of this figure is available in the online journal.)

respectively. Finally, the concentration of methane in equilibrium follows the carbon abundance. At the temperatures of GJ 436b, methane is supposed to be highly abundant in equilibrium, as shown in Figure 5, with mixing ratios of 7×10^{-4}, and 2×10^{-2} for solar and 30× solar abundances, respectively. However, CO can be enhanced and methane can be depleted to some extent due to non-equilibrium chemistry (Zahnle et al. 2009b), which will be discussed in Section 4.2 below.

The constraints due to the considerations of physical plausibility are shown in Figure 3. The gray surface shows regions assuming conservative boundaries of $\xi^2 \leqslant 3$, $CH_4 \geqslant 10^{-7}$, $CO_2 \leqslant 10^{-3}$, $H_2O \geqslant 10^{-5}$, and $CO \leqslant 10^{-1}$, while the black surfaces show a subset of the gray surface with $\xi^2 \leqslant 3$, $CH_4 \geqslant 10^{-7}$, $CO_2 \leqslant 10^{-4}$, $H_2O \geqslant 10^{-4}$, and $CO \leqslant 10^{-2}$. The black contours represent our most likely interpretation of the observations, which will be justified below. A best-fit model consistent with our constraints above is shown in Figure 4.

Our most plausible constraints on the atmosphere of GJ 436b indicate the possibility of high metallicity, along with non-equilibrium chemistry. The black surfaces in Figure 3 show that a CO abundance $\geqslant 10^{-3}$ is required to have an H_2O abundance of $\geqslant 10^{-4}$ and a methane abundance above 10^{-7}. The corresponding constraint on CO_2 is 10^{-6} to 10^{-4}. While this CO_2 abundance can be explained based on equilibrium chemistry with high metallicity alone (see Figure 5), the high CO abundance requires high metallicity along with non-equilibrium chemistry. As shown in Figure 5, very high CO abundances can exist at the bottom of the atmosphere, for high metallicity; however, the cooler upper layers of the atmosphere have much lower CO abundance. Non-equilibrium chemistry in the form of eddy mixing can transport CO from the lower layers to the upper layers of the atmosphere to cause a uniformly high CO over the entire atmosphere, as discussed in Section 3.3.2. On the other hand, the low CH_4 abundance could potentially be caused by non-equilibrium chemistry as well (Zahnle et al. 2009b). In what follows, we will explore the realm of non-equilibrium chemistry in an attempt to explain the observed constraints.

4.2. Explanations for Non-equilibrium Abundances

Our best-fit constraints on the chemical composition of GJ 436b require substantial deviations from equilibrium chemistry with solar metallicity. Non-equilibrium processes have been known to influence chemical compositions of several planetary and brown dwarf atmospheres, as discussed in Section 3.3. Here, we explore channels of non-equilibrium chemistry in search of potential explanations to the observed constraints which are inexplicable by equilibrium chemistry alone, namely, the high CO and CO_2 abundances, and the low CH_4 abundance.

4.2.1. High CO and CO_2

The high abundances of CO and CO_2 required by the observations can be achieved via eddy mixing, along with high metallicity. As explained in Section 3.3.2, eddy mixing transports CO from the deeper layers of the atmosphere to the upper layers of the atmosphere where CO is less abundant. The relevant quantity is the quench pressure (p_0), which denotes the pressure level in the atmosphere below which the rate of vertical mixing is faster than the reaction rate for chemical equilibrium; the CO concentration in the upper atmosphere ($P < p_0$) freezes at its value at $P = p_0$. Figure 6 shows the dependence of the quench level (p_0) on the diffusion coefficient (K_{zz}), for a best-fit P–T profile of GJ 436b. Higher values of K_{zz} lead to mixing of species from deeper levels of the atmosphere, i.e., higher p_0. It can be seen from the figure that K_{zz} values between 10^6 and 10^7 can cause mixing from a quench level of ∼1 bar.

The abundance of CO in the upper atmosphere depends on K_{zz} and the metallicity. The right panel of Figure 6 shows the range of CO mixing ratios that are attainable with different values of K_{zz} and metallicities. For solar metallicity, a maximum CO mixing ratio of $\sim 10^{-4}$ is attainable for K_{zz} values between $\sim 10^7$ and 10^8. However, CO mixing ratios above 10^{-3} require metallicities greater than 10× solar, and $K_{zz} \sim 10^5$ to 10^8. For a very high metallicity of 30× solar, a maximum CO mixing ratio 10^{-4} can be attained for a rather low K_{zz} of $\sim 10^3$ cm^2 s^{-1}, and a maximum of $\sim 10^{-2}$ for K_{zz} between $\sim 10^6$ and 10^8 cm^2 s^{-1}. For comparison, planetary atmospheres in the solar system have K_{zz} ranging between 10^5 and 10^9 cm^2 s^{-1} (see, e.g., Prinn & Bashay 1977; Fegley & Lodders 1994; Yung & Demore 1999), and for brown dwarf atmospheres, K_{zz} can range between 10^2 and 10^6 cm^2 s^{-1} (Saumon et al. 2006; Stephens et al. 2009).

The constraint on K_{zz} is also dependent on the choice of the characteristic length scale for mixing (L), through Equation (5). In the above results, we used the typical assumption of $L = H$, the scale height of the atmosphere (e.g., Prinn & Bashay 1977; Line et al. 2010). However, for the coolest of giant planets, like Jupiter, L can be $\sim 0.1H$ (Smith 1998). We find that a choice of $L < H$ for GJ 436b results in only a modest change in the required K_{zz}. For instance, the peak CO mixing ratio for 10× solar metallicity, for the $L = H$ case, is attained for $K_{zz} = 10^6$ to 10^8 cm^2 s^{-1}, whereas the same value for even the extreme case of $L = 0.1H$ is attained for $K_{zz} = 10^4$ to 10^6 cm^2 s^{-1}. Such differences in K_{zz} can be compensated by the uncertainty in the metallicity, as seen in Figure 6.

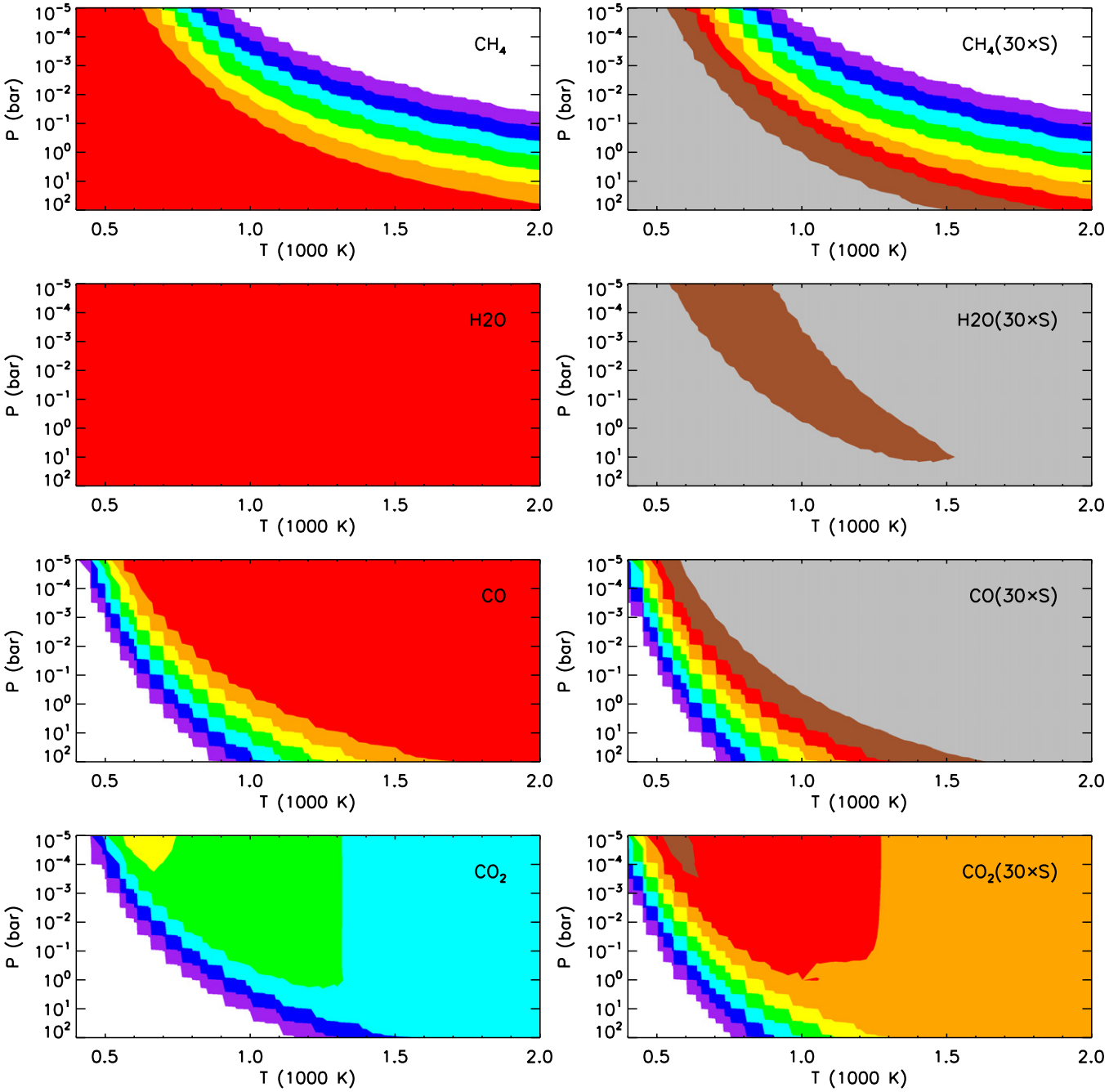

Figure 5. Concentrations of CH_4, H_2O, CO, and CO_2, predicted by equilibrium chemistry assuming solar and 30× solar elemental abundances (see Section 3.3.1). Each panel shows the contours of molecular mixing ratios (i.e., ratio by number density) with respect to molecular hydrogen, in pressure–temperature space. The left panels show mixing ratios for solar metallicity, and the right panels ("30×*S*") have 30× solar metallicity. The gray, brown, red, orange, yellow, green, cyan, blue, and purple contours correspond to mixing ratios greater than 10^{-2}, 10^{-3}, 10^{-4}, 10^{-5}, 10^{-6}, 10^{-7}, 10^{-8}, 10^{-9}, and 10^{-10}, respectively. The black lines are some of the best-fitting pressure–temperature profiles.

(A color version of this figure is available in the online journal.)

Finally, high metallicity is also consistent with the high CO_2 abundance required to explain the observations. At the quench levels of ∼1 bar, the equilibrium mixing ratio of CO_2 is 10^{-7} and 10^{-4}, for solar and 30× solar metallicity, as shown in Figure 5. The strong dependence of CO_2 on metallicity has been reported is previous studies (Lodders & Fegley 2002; Zahnle et al. 2009a), suggesting CO_2 as a key metallicity indicator. We, thus, find that a metallicity of 10–30× solar and vertical mixing of $K_{zz} \sim 10^5$ to 10^8 can simultaneously explain the constraints on CO and CO_2 observed in Section 4.1.1. The K_{zz} and metallicity are constrained further in Section 4.2.3.

4.2.2. Low CH_4

The low methane abundance required by the observations cannot be explained by equilibrium chemistry. At $P \sim 1$ bar and $T \sim 1000$ K (corresponding to the best-fitting P–T profiles), equilibrium chemistry yields methane mixing ratios of about 10^{-4} and 10^{-2} for solar and 30× solar metallicity, respectively, as shown in Figure 5. Furthermore, considering non-equilibrium thermochemistry using the CO–CH_4 reaction pathway alone, as investigated in Section 4.2.1 above, does not explain the low methane abundances. By non-equilibrium thermochemistry, we

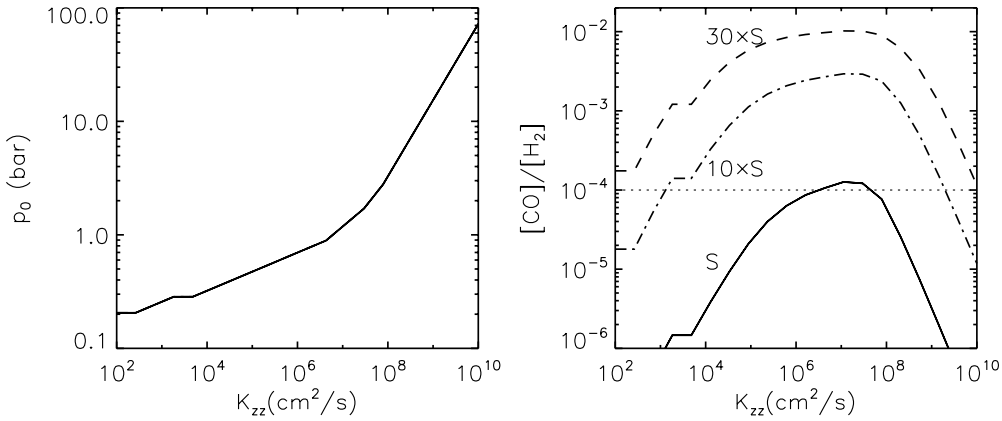

Figure 6. Vertical eddy diffusion in GJ 436b. The two panels show the dependence of the "quench" pressure (p_0) and the CO mixing ratio on the coefficient of eddy diffusion, K_{zz}. S, $10 \times S$, and $30 \times S$ refer to solar, 10 times solar, and 30 times solar metallicities.

mean departures from equilibrium chemistry due to vertical mixing. The remaining alternatives in searching for a low-methane solution include a more detailed treatment of non-equilibrium thermochemistry, including all the possible species and reactions, and photochemistry. Zahnle et al. (2009b) have reported such calculations over a range of temperatures and eddy mixing coefficients that are relevant to the current situation.

Substantial depletion of methane below equilibrium values is possible due to non-equilibrium thermochemistry and photochemistry. Full kinetics models yield a substantial amount of free radicals, especially H (Liang et al. 2003; Zahnle et al. 2009b). Zahnle et al. (2009b) show that the resultant overabundance of H leads to the depletion of methane via two main channels. At high temperatures ($T > 1200$ K), H readily reacts with H_2O to yield the reactive OH radical, which oxidizes CH_4 in very short timescales. The result is an excess production of CO. At lower temperatures ($T < 1200$ K), water is more stable, leading to a reducing environment with abundant free H. Methane, being still reactive, reacts with H to form higher hydrocarbons, and can be markedly reduced below equilibrium levels. Thus, in either scenario, the methane concentration at the observable pressure levels can be substantially depleted below equilibrium, depending on the temperature, eddy mixing coefficient (K_{zz}), metallicity, and photochemistry (Zahnle et al. 2009b).

Two key parameters governing non-equilibrium methane chemistry are the temperature and K_{zz}. The best-fitting P–T profiles required by the observations all have temperatures over 1100 K in the lower atmospheres ($P \gtrsim 10$ bar), similar to those obtained from self-consistent models of GJ 436b (Spiegel et al. 2010). Figure 7 shows a sample best-fit P–T profile (panel (A)), which has an isothermal temperature structure of 1200 K below $P \sim 1$ bar. And, as described in Section 4.2.1, the observational constraint on the CO concentration requires $K_{zz} \sim 10^7$ cm^2 s^{-1}. Panel (B) of Figure 7 shows the CO–CH_4 reaction timescale and the eddy mixing timescale, for K_{zz} of 10^7 cm^2 s^{-1}, varying with pressure; the timescales intersect at the quench pressure (p_0) of $\sim$1 bar.

The methane mixing ratios attainable via kinetics and photochemistry for the required parameters are discussed in Zahnle et al. (2009b). The parameters are: $T = 1200$ K, $K_{zz} = 10^7$ cm^2 s^{-1}, and $p_0 = 1$ bar. Panel (C) of Figure 7 shows mixing ratio profiles from our CO–CH_4 disequilibrium model (Section 4.2.1), and the mixing ratio profiles from Zahnle et al. (2009b), corresponding to the same T and K_{zz}. As shown in panel (C), their results show that $CH_4 \leqslant 10^{-7}$ is possible at the 1 bar level, assuming $5\times$ solar metallicity and a stellar irradiation that is $100\times$ the solar insolation at Earth. Lower temperatures and higher K_{zz} both favor higher methane concentration at the 1 bar level. The chemistry is less sensitive to photochemistry at higher pressures deep in the atmosphere.

4.2.3. Joint Constraints on Metallicity and Eddy Mixing

The observational constraints on all the molecules yield a plausible set of constraints on the metallicity and K_{zz}. A full kinetic and/or photochemical model is beyond the scope of the current work. However, based on the models of Zahnle et al. (2009b) with the T and K_{zz} that we constrain for GJ 436b, we find that the low methane mixing ratio (10^{-7} to 10^{-6}) observed can most likely be explained by non-equilibrium chemistry. Although such low methane abundances can be obtained for $5\times$ solar metallicity and $K_{zz} \sim 10^7$ cm^2 s^{-1}, a higher metallicity would be required to explain simultaneously the high CO and CO_2 abundances, as described in Section 4.2.1. On the other hand, too high of a metallicity, of say $30 \times$ solar, might also increase the CH_4 abundance to above the favorable levels. We therefore choose an intermediate value of $10\times$ solar which satisfies the CO and CO_2 constraints.

Based on the above reasoning, the observed chemistry in the dayside atmosphere of GJ 436b likely results from a high metallicity ($\sim 10\times$ solar) and a $K_{zz} \sim 10^6$ to 10^7 cm^2 s^{-1}. A more robust conclusion would be possible with a full kinetic + photochemical model of GJ 436b, using our best-fit P–T profile, and the appropriate UV spectrum, or flux scaling, for the host star. The present constraints indicate a significant enhancement in the metallicity of GJ 436b over that of the host star whose metallicity is known to be consistent with solar (Torres et al. 2008). Additionally, the observations constrain the C/O ratio between 0.5 and 1.0, with the most likely solutions (black surfaces in Figure 3) suggesting a C/O between $\sim$0.85 and 1. However, whether the methane depletion required by the data can be obtained in a high C/O environment, e.g., of C/O = 1, needs to be investigated by a full non-equilibrium chemistry model in the future.

4.3. Temperature Structure and Day–Night Energy Redistribution

The *Spitzer* observations provide important constraints on the vertical thermal gradient and the energy balance in the dayside atmosphere of GJ 436b. The observed brightness temperatures in the six *Spitzer* channels range from about 700 K in the 4.5 μm IRAC channel (3σ upper limit) to about 1100 K in

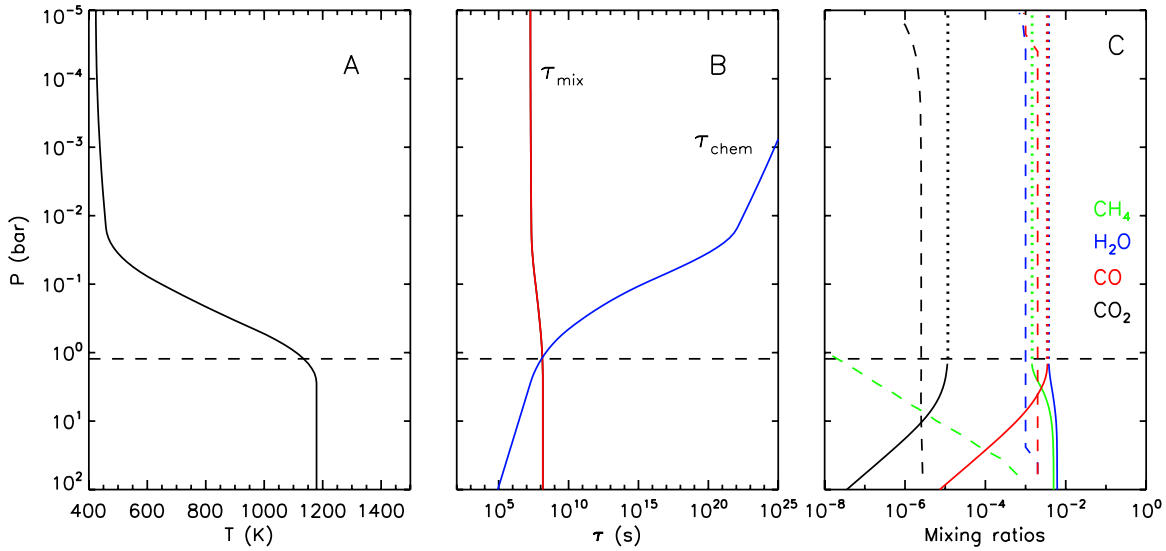

Figure 7. Non-equilibrium chemistry in GJ 436b. Panel (A) shows the pressure–temperature (P–T) profile of a best-fit model. Panel (B) shows the timescales of eddy mixing ($\tau_{\rm mix}$) and of CO–CH_4 equilibrium chemistry ($\tau_{\rm chem}$). Panel (C) shows the influence of eddy mixing on the mixing ratios of the four prominent species. The solid lines in panel (C) show the compositions from equilibrium chemistry, which continue as dotted lines above the quench level, and fixed to the values at the quench level. The dashed lines show the mixing ratios from Zahnle et al. (2009b), for an isothermal atmosphere with $T = 1200$ K, $K_{zz} = 10^7$ cm^2 s^{-1}, and 5× solar metallicity, which yields a CH_4 mixing ratio below 10^{-6} at the $P = 1$ bar level. The y-axis in all the panels is the pressure in bars. The horizontal black dashed line in all the panels show the quenching pressure level.

(A color version of this figure is available in the online journal.)

the 3.6 μm channel (Stevenson et al. 2010). With the exception of the 3.6 μm IRAC channel, observations in all the remaining five channels are consistent with a blackbody planet spectrum at 750 K ± 100 K. However, the 3.6 μm observation of ∼1100 K brightness temperature is a major exception, requiring a temperature differential of ∼400 K between the 3.6 μm and 4.5 μm channels, implying a very steep temperature gradient in the atmosphere. The dayside pressure–temperature (P–T) profiles of GJ 436b constrained by the observations are shown in Figure 2. The best-fitting P–T profiles (in purple) have temperatures varying by over ∼400 K per bar of pressure in the lower atmosphere, required primarily by the large temperature differential described above.

The observations rule out the presence of a significant thermal inversion in the dayside atmosphere of GJ 436b. Our results show that the observations cannot be fit with an inversion model for any chemical composition (although very small inversions which might cause only weak observable features cannot be ruled out by present data). A significant thermal inversion in this atmosphere would have caused the brightness temperatures in the 4.5, 5.8, and 8 μm channels to be markedly higher than the 3.6 μm channel, much higher than what the current data indicate. Finally, as has been known for all hot Jupiters, the data indicate that the observable dayside atmosphere of GJ 436b is mostly radiative, with the radiative zones of some of the best-fitting P–T profiles extending to pressures above ∼10 bar. The isotherms at the high pressure ends of the P–T profiles are suggestive of the radiative diffusion approximation in the high optical depth limit (see, e.g., Madhusudhan & Seager 2009) and are also found in other self-consistent models reported in the literature (e.g., Spiegel et al. 2010).

The large brightness temperature of 1100 K observed in the 3.6 μm channel is also indicative of low day–night energy redistribution in GJ 436b. The 3.6 μm channel probes levels deep in the atmosphere (around pressures of 1 bar or higher). A high 3.6 μm brightness temperature, therefore, indicates a high blackbody continuum emerging from the base of the dayside atmosphere at ∼1 bar. Our best-fit models show that the net emergent flux on the day side nearly balances the incident stellar flux, implying that very little energy is circulated to the night side. The bottom-right panel of Figure 3 shows that the ξ^2 contours in $\eta = (1 - A)(1 - f_r)$ and $T_{\rm eff}$. $\eta = (1 - A)(1 - f_r)$ are obtained from energy balance, where A is the bond albedo and f_r is fraction of energy redistributed to the night side (Madhusudhan & Seager 2009).

The best-fitting models favor $\eta \gtrsim 0.75$, or a maximum day–night redistribution (f_r) of 0.25, i.e., for $A = 0$. An albedo of, say 0.1, further restricts the distribution to 0.2. Our results support similar conclusions arrived at by previous works (Deming et al. 2007; Spiegel et al. 2010). It is to be noted that we do not assume uniform illumination of the planetary day side by the stellar irradiation (i.e., weighing the stellar flux by $f = \frac{1}{2}$). Instead, we use $f = \frac{2}{3}$, according to the prescription of Burrows et al. (2008), which is also used in Madhusudhan & Seager (2009). Consequently, our $T_{\rm eff}$ estimate for a given η is typically higher than one would obtain using the $f = \frac{1}{2}$ assumption.

Our conclusion of a low day–night redistribution on this planet assumes special significance for potential future observations of thermal phase curves of GJ 436b. Thermal phase curves in the 3.6 μm and 4.5 μm IRAC channels, feasible with warm *Spitzer*, should show clear model-independent evidence of a high day–night temperature contrast, according to our present results. A finding on the contrary, i.e., finding efficient redistribution in the phase curves, can imply the possibility of a substantial interior energy source in GJ 436b.

5. DISCUSSION AND SUMMARY

We presented a detailed analysis of the dayside atmosphere of GJ 436b. Our results show that a high metallicity along with non-equilibrium chemistry are required to explain the observations. We also studied the correlations between the various molecular species, and reported detailed constraints on the metallicity,

chemical processes, and day–night energy circulation. Although our results come from observations in six channels of *Spitzer* photometry, some channels are more important than others. Here, we discuss the relative importance of the different *Sptizer* channels to our conclusions. We also discuss some potential alternate interpretations of the data, followed by a summary of our results.

5.1. Sensitivity of Results to Spitzer Observations

The constraints reported in this work depend critically on the two *Spitzer* IRAC observations at 3.6 μm and 4.5 μm. The high planet–star flux contrast in the 3.6 μm channel is responsible for the constraints of low methane abundance and low energy circulation. The low flux contrast in the 4.5 μm channel is responsible for the requirement of high CO and/or CO_2 in GJ 436b. While the observation in the 3.6 μm channel was reported to be of the highest S/N of all channels, the 4.5 μm channel was a non-detection (Stevenson et al. 2010). Nevertheless, future observations in both these channels would be extremely important to confirm that these fluxes actually represent the steady state atmosphere in GJ 436b. The observations in the remaining four channels (5.8–24 μm) are much less constraining, although still very useful. For instance, the moderate flux observed in the 8 μm channel, where methane absorbs strongly, is important to the conclusion that the very high flux in the 3.6 μm channel could not have been due to a thermal inversion causing methane emission.

Our constraints on the molecular abundances are fairly robust with respect to the observational uncertainties. The high flux in the 3.6 μm channel cannot be explained by equilibrium chemistry. A model with equilibrium chemistry and solar or 30× solar metallicities predicts planet–star flux contrasts that are lower than the observed value by over 4σ (also in agreement with models of Demory et al. 2007 and Spiegel et al. 2010). On the other hand, the contrasts predicted in the 4.5 μm channel based on equilibrium chemistry alone would be higher than the observed non-detection by over 3σ (also see Spiegel et al. 2010). We have been conservative in our analysis by allowing our best fits to the 4.5 μm point to lie within the $3\sigma \pm 1\sigma$ upper limits. Had we considered this point to be a strict non-detection at 1σ, our results would predict even higher CO and/or CO_2. Finally, the large uncertainties in the observed fluxes in the 16 μm and 24 μm channels provide only fiducial constraints on the temperature structure and the H_2O and CO_2 abundances.

5.2. Alternate Interpretations

The high planet–star flux contrast observed in the 3.6 μm IRAC channel is central to most of the constraints reported in this work. Our inferences could partly be restricted by the specific choices that are inherent to our models. For example, our models do not include clouds or hazes. Although scattering from hazes has been suggested to be potentially relevant in the optical and near-IR (e.g., Sing et al. 2009), a high contribution at the longer wavelengths of the 3.6 μm channel is unlikely. We have also assumed the planet atmosphere to be in local thermodynamic equilibrium (LTE). Swain et al. (2010) reported a potential signature due to non-LTE methane fluorescent emission in HD 189733b observed in the range of the 3.6 μm channel (but cf. Mandell et al. 2010, who did not find such a feature in follow-up observations). The dayside atmosphere of GJ 436b might also be variable, as has been reported previously for hot Jupiters (Grillmair et al. 2008; Madhusudhan & Seager 2009). However, for variability to explain the observed flux in the 3.6 μm channel, the temperature at the ∼1 bar level in the atmosphere of GJ 436b has to exhibit fluctuations greater than 400 K, between subsequent observations of Stevenson et al. (2010). These and other alternate explanations are worth exploring with more data at different epochs.

5.3. Summary

We have presented constraints on the chemical composition and temperature structure of the dayside atmosphere of hot-Neptune GJ 436b, based on recent *Spitzer* observations. One of our key findings is the strict upper limit on the mixing ratio of methane. We find that models fitting the observations require a methane mixing ratio below 10^{-6}. Slightly higher methane mixing ratios require $CO_2 \sim 10^{-3}$ to 10^{-2}, which is implausible in the hydrogen rich atmosphere with the temperature structure of GJ 436b. The abundances of all the molecules are highly correlated. Applying nominal conditions of physical plausibility, we find the constraints on the molecular mixing ratios to be $CH_4 \sim 10^{-7}$ to 10^{-6}, CO $\geqslant 10^{-3}$, $CO_2 \sim 10^{-6}$ to 10^{-4}, and $H_2O \leqslant 10^{-4}$. These constraints on the molecular abundances cannot all be explained based on equilibrium chemistry, for any metallicity, as reported in Stevenson et al. (2010). At the temperatures of GJ 436b, equilibrium chemistry with solar abundances predicts CH_4, CO, and CO_2 mixing ratios to be $\sim 5 \times 10^{-4}$, $\sim 10^{-5}$ and $\sim 10^{-7}$, respectively, contrary to the observed abundances.

The observed constraints on the molecular abundances can be explained by a combination of high metallicity and non-equilibrium thermochemistry. A high metallicity is required for a high CO_2 abundance. Vertical mixing along with high metallicity is required to dredge up the high CO abundance from the lower layers of the atmosphere to observable layers. Finally, vertical mixing and photochemistry can cause substantial depletion of CH_4, as reported by Zahnle et al. (2009b). At the temperatures ($T > 1100$ K) we obtain for the lower atmosphere of GJ 436b, the results of Zahnle et al. (2009b) indicate the depletion of equilibrium CH_4 via oxidation to CO, caused by an overabundance of the H radical. Our joint analysis of the parameters of non-equilibrium chemistry required us to explain the abundances of all the species, suggesting that the dayside atmosphere of GJ 436b has a high metallicity of ∼10× solar and a diffusion coefficient of $K_{zz} = 10^6$–10^7 cm^2 s^{-1}. The metallicity is substantially enhanced over that of the host star which is consistent with solar metallicity (Torres et al. 2008).

Our results also constrain the dayside temperature structure and the day–night energy redistribution in the atmosphere of GJ 436b. A temperature inversion is ruled out by the current observations, although small inversions which are not observable at the resolution of the current photometric data cannot be conclusively ruled out. The observations also suggest inefficient day–night energy redistribution (f_r) in GJ 436b, requiring $(1 - A_B)(1 - f_r) = \eta \geqslant 0.7$, at the 1$\sigma$ fit. Thus, the maximum f_r allowed by the data at the 1σ fits is 0.3 for zero bond albedo (A_B), and 0.23 for $A_B = 0.1$. Future observations of thermal phase curves in the available warm *Spitzer* channels will be instrumental in validating the low redistribution requirement. A finding on the contrary might indicate a substantial interior energy source. We emphasize that the constraints reported in this work depend primarily on the two *Spitzer* channels (3.6 μm and 4.5 μm). Thus, future observations in these channels will be extremely important in confirming the present and previous results on the atmosphere of GJ 436b.

The atmosphere of the hot-Neptune GJ 436b presents new challenges and opportunities for detailed modeling of exoplanet atmospheres. As low-mass transiting planets continue to be discovered, unexpected findings are likely to continue. The next generation of models and observations will help unravel those mysteries and help put our solar system in perspective.

N.M. thanks Adam Showman, James Kasting, Julianne Moses, Channon Visscher, David Spiegel, Jonathan Fortney, Ivan Hubeny, Olivier Mousis, and Mark Marley for helpful discussions. We thank Richard Freedman for providing molecular line lists, especially with helpful information on CO_2 opacities. We thank Larry Rothman for access to the HITEMP database. We thank the MIT Kavli Institute for facilitating access to the computer cluster used for this work. Support for this work was provided by NASA through an award issued by JPL/Caltech.

REFERENCES

Bakos, G., et al. 2010, ApJ, 710, L1724
Barman, T. S. 2007, ApJ, 661, L191
Barman, T. S., Hauschildt, P. H., & Allard, F. 2005, ApJ, 632, 1132
Borucki, W. J., et al. 2010, ApJ, 713, L126
Borysow, A. 2002, A&A, 390, 779
Borysow, A., Jorgensen, U. G., & Zheng, C. 1997, A&A, 324, 185
Burrows, A., Budaj, J., & Hubeny, I. 2008, ApJ, 678, 1436
Burrows, A., Hubeny, I., Budaj, J., Knutson, H. A., & Charbonneau, D. 2007, ApJ, 668, L171
Burrows, A., & Sharp, C. M. 1999, ApJ, 512, 843
Burrows, A., Sudarsky, D., & Hubeny, I. 2006, ApJ, 650, 1140
Butler, R. P., Vogt, S. S., Marcy, G. W., Fischer, D. A., Wright, J. T., Henry, G. W., Laughlin, G., & Lissauer, J. J. 2004, ApJ, 617, 580
Charbonneau, D., Brown, T. M., Noyes, R. W., & Gilliland, R. L. 2002, ApJ, 568, 377
Charbonneau, D., Knutson, H. A., Barman, T., Allen, L. E., Mayor, M., Megeath, S. T., Queloz, D., & Udry, S. 2008, ApJ, 686, 1341
Charbonneau, D., et al. 2005, ApJ, 626, 523
Charbonneau, D., et al. 2009, Nature, 462, 891
Cooper, C. S., & Showman, A. P. 2006, ApJ, 649, 1048
Deming, D., Harrington, J., Laughlin, G., Seager, S., Navarro, S. B., Bowman, W. C., & Horning, K. 2007, ApJ, 667, L199
Deming, D., Seager, S., Richardson, L. J., & Harrington, J. 2005, Nature, 434, 740
Demory, B., et al. 2007, A&A, 475, 1125
Desert, J-M., Lecavelier des Etangs, A., Hebrard, G., Sing, D. K., Ehrenreich, D., Ferlet, R., & Vidal-Madjar, A. 2009, ApJ, 699, 478
Fegley, B., & Lodders, K. 1994, Icarus, 110, 117
Figueira, P., Pont, F., Mordasini, C., Alibert, Y., Georgy, C., & Benz, W. 2009, A&A, 493, 671
Ford, E. 2005, AJ, 129, 1706
Fortney, J. J., Saumon, D., Marley, M. S., Lodders, K., & Freedman, R. S. 2006, ApJ, 642, 495
Freedman, R. S., Marley, M. S., & Lodders, K. 2008, ApJS, 174, 504
Gillon, M., et al. 2007, A&A, 471, 51
Griffith, C. A., & Yelle, R. V. 1999, ApJ, 519, L85
Grillmair, C. J., et al. 2008, Nature, 456, 767
Hartman, J. D., et al. 2010, arXiv:1010.1008
Hubeny, I., & Burrows, A. 2007, ApJ, 669, 1248
Knutson, H. A., Charbonneau, D., Allen, L. E., Burrows, A., & Megeath, S. T. 2008, ApJ, 673, 526
Leger, A., et al. 2009, A&A, 506, 287L
Liang, M.-C., Parkinson, C. D., Lee, A. Y.-T., Yung, Y. L., & Seager, S. 2003, ApJ, 596, L247
Line, M. R., Liang, M.-C., & Yung, Y. L. 2010, ApJ, 717, 496
Lodders, K., & Fegley, B. 2002, Icarus, 155, 393
Madhusudhan, N., & Seager, S. 2009, ApJ, 707, 24
Madhusudhan, N., & Seager, S. 2010, ApJ, 725, 261
Mandell, A. M., Deming, L. D., Blake, G. A., Knutson, H. A., Mumma, M. J., Villanueva, G. L., & Salyk, C. 2010, ApJ, in press, (arXiv:1011.5507)
Maness, H. L., Marcy, G. W., Ford, E. B., Hauschildt, P. H., Shreve, A. T., Basri, G. B., Butler, R. P., & Vogt, S. S. 2007, PASP, 119, 90
Miller-Ricci, E., Seager, S., & Sasselov, D. 2009, ApJ, 690, 1056
Noll, K. S., Geballe, T. R., & Marley, M. S. 1997, ApJ, 489L, 87N
Pont, F., Gilliland, R. L., Knutson, H., Holman, M., & Charbonneau, D. 2009, MNRAS, 393, L6
Prinn, R. G., & Barshay, S. S. 1977, Science, 198, 1031
Rogers, L., & Seager, S. 2009, ApJ, 712, 974
Rothman, L. S., et al. 2005, J. Quant. Spectrosc. Radiat. Transfer, 96, 139
Saumon, D., Marley, M. S., Lodders, K., & Freedman, R. S. 2003, in IAU Symp. 211, Brown Dwarfs, ed. E. Martín (San Francisco, CA: ASP), 345
Saumon, D., Marley, M. S., Cushing, M. C., Leggett, S. K., Roellig, T. L., Lodders, K., & Freedman, R. S. 2006, ApJ, 647, 552
Seager, S., Richardson, L. J., Hansen, B. M. S., Menou, K., Cho, J. Y.-K., & Deming, D. 2005, ApJ, 632, 1122
Seager, S., & Sasselov, D. D. 2000, ApJ, 537, L916
Seager, S., Whitney, B. A., & Sasselov, D. D. 2000, ApJ, 540, 504
Sharp, C. M., & Huebner, W. F. 1990, ApJS, 72, 417
Showman, A. P., Fortney, J. J., Lian, Y., Marley, M. S., Freedman, R. S., Knutson, H. A., & Charbonneau, D. 2009, ApJ, 699, 564
Sing, D. K., Desert, J.-M., Lecavelier Des Etangs, A., Ballester, G. E., Vidal-Madjar, A., Parmentier, V., Hebrard, G., & Henry, G. W. 2009, A&A, 505, 891
Smith, M. D. 1998, Icarus, 132, 176
Spiegel, D. S., Burrows, A., Ibgui, L., Hubeny, I., & Milsom, J. A. 2010, ApJ, 709, 149
Stephens, D. C., et al. 2009, ApJ, 702, 154
Stevenson, K., et al. 2010, Nature, 464, 1161
Swain, M. R., Vasisht, G., & Tinetti, G. 2008, Nature, 452, 329
Swain, M. R., Vasisht, G., Tinetti, G., Bouwman, J., Chen, Pin, Yung, Y., Deming, D., & Deroo, P. 2009a, ApJ, 690, L114
Swain, M. R., et al. 2009b, ApJ, 704, 1616
Swain, M. R., et al. 2010, Nature, 463, 637
Tegmark, M., et al. 2004, Phys. Rev. D, 69, 103501
Tinetti, G., et al. 2007, Nature, 448, 169
Torres, G., Winn, J. N., & Holman, M. J. 2008, ApJ, 677, 1324
Visscher, C., Moses, J. I., & Saslow, S. A. 2010, Icarus, 209, 602
White, W. B., Johnson, S. M., & Dantzig, G. B. 1958, J. Chem. Phys., 28, 751
Yung, Y., & Demore, W. B. 1999, Photochemistry of Planetary Atmospheres (New York: Oxford Univ. Press)
Yung, Y. L., Drew, W. A., Pinto, J. P., & Friedl, R. R. 1988, Icarus, 73, 516
Zahnle, K., Marley, M. S., & Fortney, J. J. 2009a, arXiv:0911.0728
Zahnle, K., Marley, M. S., Lodders, K., & Fortney, J. J. 2009b, ApJ, 701, L20